J Mater Sci: Mater Electron (2022) 33:683–689

Antiferroelectric $NaNbO_3$ ceramics prepared by hydrothermal-assisted cold sintering process

Wenbin Huang[1] and Hongbo Liu[1,*]

[1] School of Materials Engineering, Shanghai University of Engineering Science, Shanghai 201620, China

Received: 4 August 2021
Accepted: 2 November 2021
Published online: 11 November 2021

ABSTRACT

A hydrothermal-assisted cold sintering process is developed for preparing antiferroelectric $NaNbO_3$ ceramic. The novel process includes hydrothermal synthesizing $NaNbO_3$ particles, cold sintering, and annealing. The physical and electrical properties of the cold sintered ceramics were studied comprehensively and compared with ceramics prepared by conventional sintering techniques. At optimum conditions, dense ceramic can be prepared by the cold sintering process with very low heat treatment temperature, and the properties are comparable with that prepared by conventional sintering.

1 Introduction

Dielectric materials have been paid great attention recently for applications in electrical energy storage [1–4]. Among them, antiferroelectric materials can store more energy than linear dielectric and ferroelectric materials with minimal losses [5–8]. However, most antiferroelectric materials are $PbZrO_3$ based compounds with a high content of toxic element Pb. To reduce environmental hazards, lead-free antiferroelectric materials like $AgNbO_3$ and $NaNbO_3$ based have been studied extensively [9–11]. Generally, $AgNbO_3$ ceramics are sintered with an O_2 atmosphere, which increases the complexity of processing. In comparison with $AgNbO_3$, the cost of raw materials for preparing $NaNbO_3$ is lower and the protective atmosphere is not necessary. Particularly, $NaNbO_3$ based solid solutions have been extensively studied to stabilize the poor antiferroelectricity of $NaNbO_3$. For instance, $x CaZrO_3$–$(1 - x)NaNbO_3$ ($0.02 \leq x \leq 0.05$) ceramics show double polarization hysteresis loops at room temperature [12] and $0.24(Bi_{0.5}Na_{0.5})TiO_3$–$0.76NaNbO_3$ ceramic achieves ultrahigh-energy storage density [13].

$NaNbO_3$ ceramics are commonly prepared by the conventional sintering technique. The densification involves multiple steps, an initial evaporation/condensation and surface diffusion up to ~ 950 °C, followed by grain boundary diffusion between 950 °C and 1150 °C, and the optimum sintering temperature is ~ 1350 °C [14]. Since the vapor pressure of saturated sodium varies from 0.2 to 18 atm when temperature increases from 727 to 1327 °C [15] and high volatility of the alkali oxides [16], the volatilization of Na during conventional sintering is inevitable, which can be inhibited by a low oxygen partial pressure during calcination and sintering [17].

Address correspondence to E-mail: bohongliu@gmail.com

https://doi.org/10.1007/s10854-021-07336-w

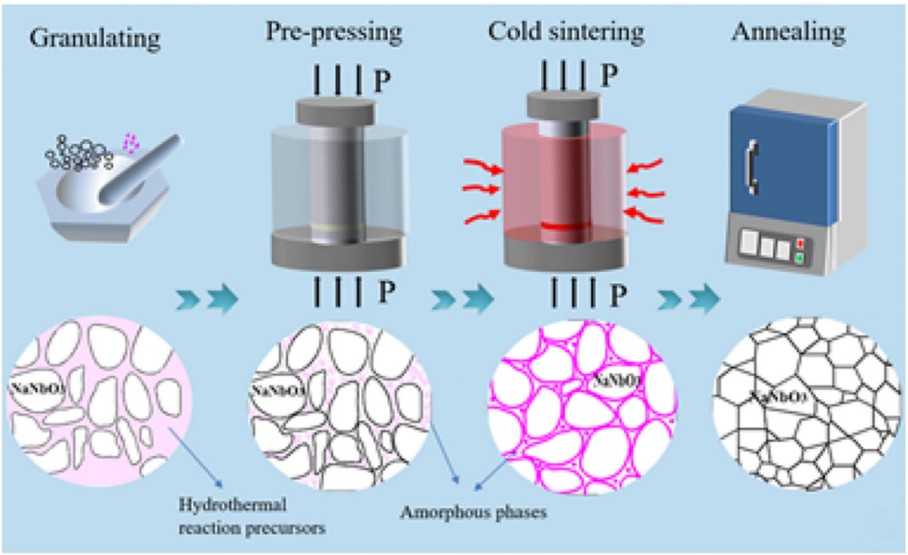

Fig. 1 Schematic illustration of cold sintering and microstructural evolution

Since the cold sintering process has been developed recently [18, 19] and $AgNbO_3$ ceramics can be sintered in ambient conditions by using hydrothermal-synthesized powders [20], a hydrothermal-assisted cold sintering process was designed to prepare $NaNbO_3$ ceramic. First, $NaNbO_3$ powders were synthesized by a hydrothermal method. Then, the ceramic green bodies were densified by a cold sintering process. Finally, the densities of the ceramics were further improved by annealing. The advantage of the novel method is that $NaNbO_3$ ceramics can be sintered at low-temperature to avoid the volatilization of Na at high-temperature during conventional sintering. Although cold sintering has been applied to preparing $NaNbO_3$ [21], the annealing temperature of this work is very low since the hydrothermal-synthesized powders were used. In this work, $NaNbO_3$ ceramics were also prepared by conventional sintering technique using the above hydrothermally synthesized powers (abbreviated HCS), and conventional sintering technique using solid-state reaction synthesized powders (abbreviated CS) to disclose the origin related to the low annealing temperature and highlight the priority of the novel process.

2 Experimental

$NaNbO_3$ powders were first synthesized by a hydrothermal method. Nb_2O_5 was weighted and dissolved in NaOH solution with a Nb_2O_5:NaOH molar ratio of 1:10. The mixed solution was then sealed in a 100 ml stainless steel reactor lined with polytetrafluoroethylene (ZKY-100 ml, Xi'an Hongchen Instrument Factory) and heated at 180 °C for 10 h. The produced precipitation was washed repeatedly with absolute ethanol and then dried to get $NaNbO_3$ powders.

The cold sintering process is shown in Fig. 1. The hydrothermal-synthesized $NaNbO_3$ powders were mixed with 10 wt% of the above-mentioned hydrothermal solution. The mixture was placed in a die and subjected to uniaxial pressures of 300–600 MPa at room temperature for 10 min, then heated to 200 °C, and kept for 1 h. The samples were then baked at 120 °C for 12 h to remove possible solution residues and annealed at 700–1000 °C for 4 h to further densification. During the cold sintering, the redistribution and diffusion of hydrothermal reaction precursors, the solution-precipitation, and mass transport of ionic species and/or atomic clusters densify green bodies. The final annealing promotes densification through the crystallization of the residual amorphous phases and the growth of crystal grains.

The ceramic prepared by HCS was sintered at 1250 °C for 3 h while the ceramic prepared by CS was sintered at 1325 °C for 3 h. For CS, Na_2CO_3 (99.0%, Macklin) and Nb_2O_5 (99.5%, Macklin) were used for synthesizing $NaNbO_3$ powders. The raw materials were mixed in a stoichiometric ratio and homogenized in a planetary mill for 12 h using ethanol as the

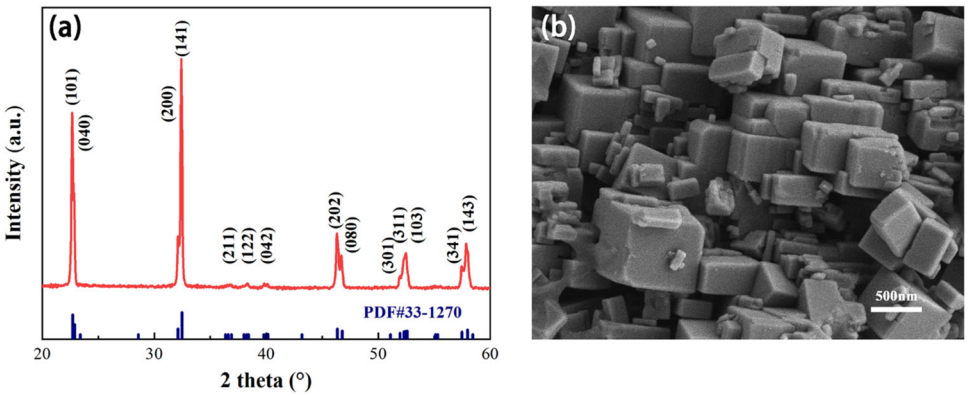

Fig. 2 The X-ray diffraction pattern (**a**) and microstructural image (**b**) of hydrothermal-synthesized $NaNbO_3$

liquid medium. The mixed powders were calcined at 950 °C for 3 h, and then ball-milled for 12 h again.

The densities of the ceramics were measured by the Archimedes method using deionized water as a liquid medium, a theoretical density of 4.58 g/cm^3 was adopted for calculating the relative densities. The crystal structures were examined by an X-ray diffraction Diffractometer (PANalytical X'Pert PRO). All samples were surface polished and thermally etched before ceramographic analysis. The microstructures were observed by a scanning electron microscope (TESCAN-VEGA3) using the secondary electron imaging mode. The dielectric properties were measured by an impedance analyzer (Keysight E4990A) at 1 kHz–1 MHz from room temperature to 500 °C with a heating rate of 3°C/min. The room temperature polarization–electric field (P–E) hysteresis loops were measured at 10 Hz by a commercial ferroelectric tester (Radiant Technology Precision LC II). The thicknesses of the samples for P–E measurement are around 0.2 mm.

3 Results and discussion

X-ray diffraction pattern of the hydrothermal-synthesized powders is shown in Fig. 2a. The diffraction peaks can be indexed by a standard X-ray diffraction powder diffraction pattern (JCPDS, 33-1270) of $NaNbO_3$, indicating $NaNbO_3$ in pure phase was synthesized. The synthesized particles are cubes with the size varying from 200 to 500 nm as shown in Fig. 2b by the scanning electron microscope image.

The relative densities of prepared ceramics are shown in Fig. 3. For cold sintered ceramics, when the applied pressure varies from 300 to 600 MPa, the density increases first then decreases slightly, and 500 MPa is the optimum pressure. The density also

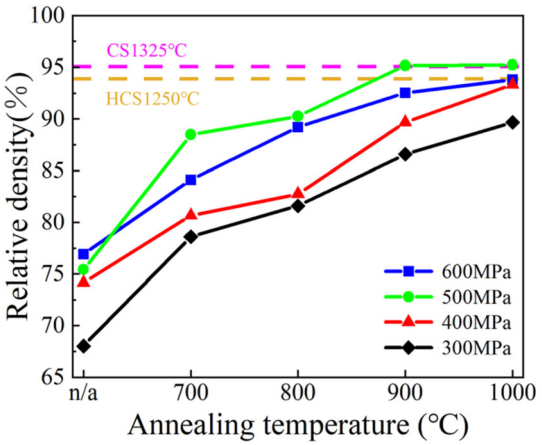

Fig. 3 The relative densities of the prepared $NaNbO_3$ ceramics with different uniaxial pressures and annealing temperatures. The densities of green bodies (with the abscissa of "n/a"), and ceramics prepared by CS and HCS (shown by horizontal lines) are also included

increases with increasing annealing temperature. Since at 500 MPa after 900 °C the benefit is negligible from increasing annealing temperature, the optimum annealing temperature is 900 °C. The relative density is 95% for a ceramic cold sintered at 500 MPa and annealed at 900 °C. As also shown in Fig. 3, the relative density is 95% for CS prepared ceramic and is 94% for HCS prepared ceramic. Similar values are reported, e. g., the relative density is 95% (recalculated with a theoretical density of 4.58 g/cm^3) for CS sintered ceramic (1355 °C for 3.5 h) [22], the relative density is 94.4% for CS sintered ceramic (1250 °C for 2 h) using chemical route synthesized powders [23]. Thus, the advantage of hydrothermal-assisted cold sintering is the low heat-treatment temperature (900 °C) in comparison with other methods. Since the annealing temperature is 1230 °C for cold sintered ceramic using solid-state reaction synthesized powders [21], the low heat-treatment temperature of the

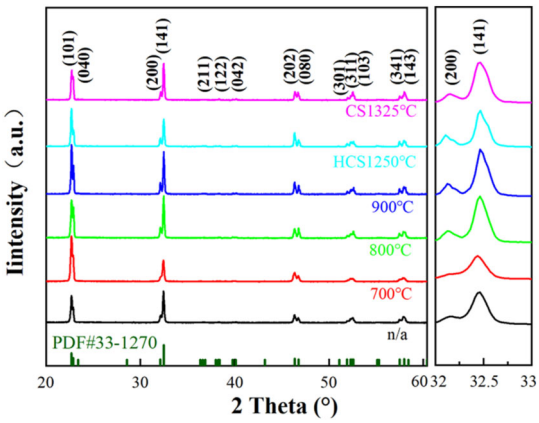

Fig. 4 X-ray diffraction patterns of the cold sintered, HCS, and CS prepared ceramics. "n/a" means without annealing, other values are annealing temperatures. The right inset is the enlarged (200) and (141) diffraction peaks

novel process is partly due to the small size of the hydrothermal-synthesized powders as shown in Fig. 2b.

The X-ray diffraction patterns of the cold sintering, HCS, and CS prepared ceramics are shown in Fig. 4. The diffraction peaks can be indexed by a standard X-ray diffraction powder diffraction pattern (JCPDS, 33-1270) of $NaNbO_3$. The diffraction peaks of cold sintered ceramics become sharper with increasing the annealing temperature as shown by (200) and (141) peaks in the right inset of Fig. 4. Since during the cold sintering the surface ions of $NaNbO_3$ particles dissolve into the solution first and then precipitate again, the dissolution–precipitation process forms amorphous phases. Thus, residual amorphous phases exist after cold sintering, the annealing promotes the crystallization of the residual amorphous phases, which makes the diffraction peaks sharper.

The microstructural images of prepared ceramics are shown in Fig. 5. The unannealed ceramic has residual amorphous phases filled between grains (Fig. 5a). The content of the residual amorphous phases gradually decreases with increasing the annealing temperature (Fig. 5b, c). Finally, the 900 °C annealed ceramic (Fig. 5d) has a similar microstructure to that of HCS and CS prepared ceramics (Fig. 5e–f). The averaged grain size is 0.7 μm, 1.3 μm, 1.7 μm, 1.8 μm, and 2.5 μm for 700 °C, 800 °C, 900 °C annealed, HCS, and CS prepared ceramics.

The frequency-dependent dielectric properties of the prepared ceramics are shown in Fig. 6. For cold sintered ceramics unannealed or annealed at 700 °C, the dielectric loss is very high and the dielectric constant decreases significantly with frequency, indicating a large contribution from structure-defect-related space charge dielectric relaxation [24]. The dielectric loss of the cold sintered ceramics annealed at 800 °C and 900 °C decreases significantly and the dielectric constant is almost constant with frequency. Particularly, the dielectric properties of the cold

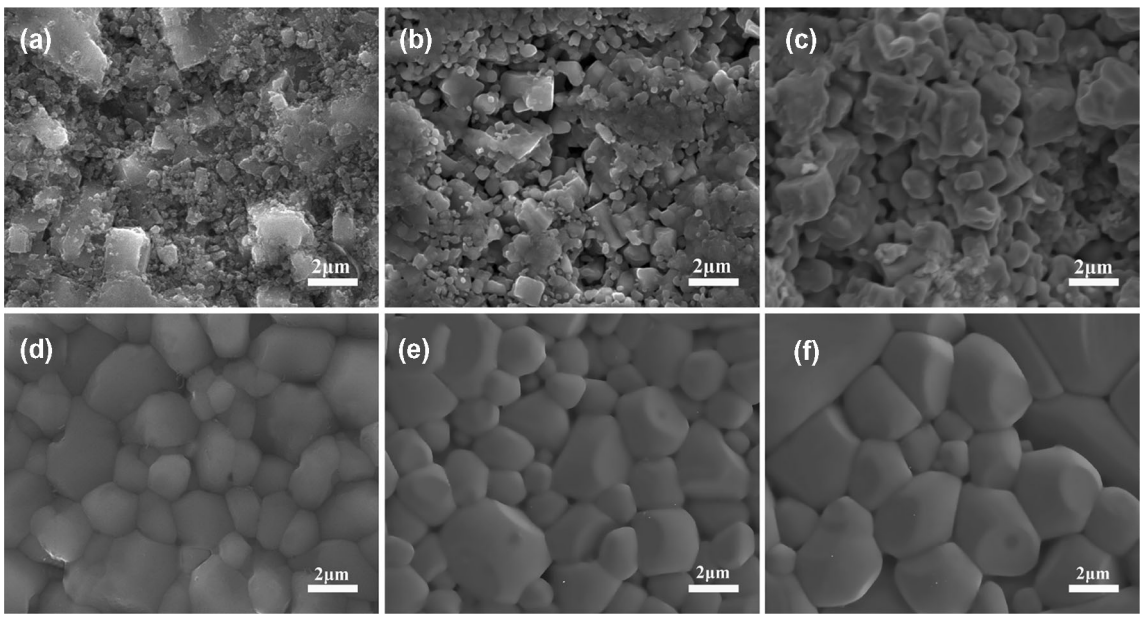

Fig. 5 Scanning electron microscope images of prepared ceramics. **a** Cold sintered without annealing; **b** cold sintered with annealing at 700 °C; **c** cold sintered with annealing at 800 °C; **d** cold sintered with annealing at 900 °C; **e** HCS prepared; **f** CS prepared

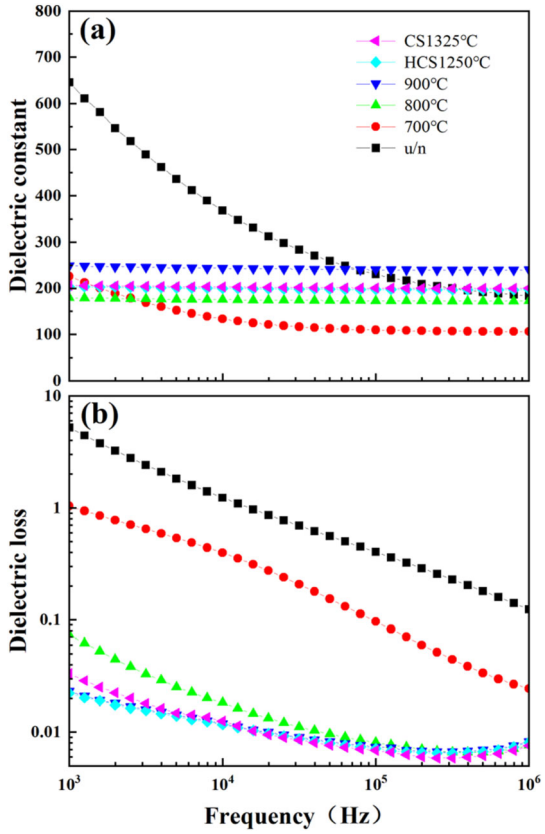

Fig. 6 Frequency-dependent dielectric constant (**a**) and dielectric loss (**b**) of ceramics prepared by cold sintering, HCS, and CS

sintering ceramic annealed at 900 °C are similar to that of HCS and CS prepared ceramics.

The temperature-dependent dielectric properties are shown in Fig. 7. The dielectric peak is hard to be seen for unannealed ceramic but becomes sharper with increasing annealing temperature. At the same time, the dielectric loss decreases significantly after annealing, once again indicating the suppression of structure-defect-related space charge dielectric relaxation.

$NaNbO_3$ undergoes a complex phase transition sequence [25–28]. In the temperature-dependent dielectric spectrum, the main dielectric anomaly is attributed to the structural phase transition from orthorhombic P phase to orthorhombic R phase on heating [9]. As shown in Fig. 7g, the temperature of the main dielectric anomaly is sensitive to the preparing process, it increases with increasing the annealing temperature, has the same value for 900 °C annealed ceramic and HCS prepared ceramic and gets the highest value for CS prepared ceramic. By referring to the grain size in Fig. 5, the phenomenon is consistent with the result that the P–R phase transition is size-dependent, and a ceramic with a larger grain size has a higher temperature of the P–R phase transition [29].

There is another weak dielectric anomaly at around 195 °C for 900 °C annealed, HCS, and CS prepared ceramics as shown in Fig. 7i. For qualitatively defining this transition, the derivative of the dielectric constant versus temperature was calculated as suggested [8]. The result indicates that the phase transition starts at 173 °C, indicating that the origin of this anomaly was attributed to the transition to an incommensurate phase [30, 31].

The P-E loops are shown in Fig. 8. The polarization of 900 °C annealed ceramic is higher than HCS and CS prepared ceramics. The maximum polarization intensity is 19 $\mu C/cm^2$. The remanent polarization is 15 $\mu C/cm^2$, which is the same as a ceramic prepared by using molten salt synthesized nanoparticles [32] and comparable with that of single crystals [33]. Instead of double P–E loops, the typical ferroelectric hysteresis loops are observed for all ceramics when the applied electric field is higher than 50 kV/cm. This is not unnormal since in most cases only ferroelectric hysteresis loops were measured [12, 17, 21, 31, 32, 34]. Although the initial electric field from antiferroelectric P to the ferroelectric Q phase (space group $P2_1ma$) is ~ 110 kV/cm, the ferroelectric P–E loop was obtained during the second cycle with the coercive field of ~ 40 kV/cm [10, 22]. It is proposed that the ferroelectric state is only slightly less stable than the antiferroelectric state [35, 36] and quite stable with time [34, 37].

4 Conclusions

$NaNbO_3$ ceramics were successfully prepared by a hydrothermal-assisted cold sintering process. The physical and electrical properties of cold sintered ceramic were compared with that prepared by HCS and CS process. The advantage of the novel process is the low heat-treatment temperature. A ceramic cold sintered at 200 °C and 500 MPa for 1 h with annealing at 900 °C for 4 h has similar properties with ceramics prepared by HCS at 1250 °C for 3 h and CS at 1325 °C for 3 h. The work establishes a fundamental methodology to prepare $NaNbO_3$ based ceramics at extremely low temperatures.

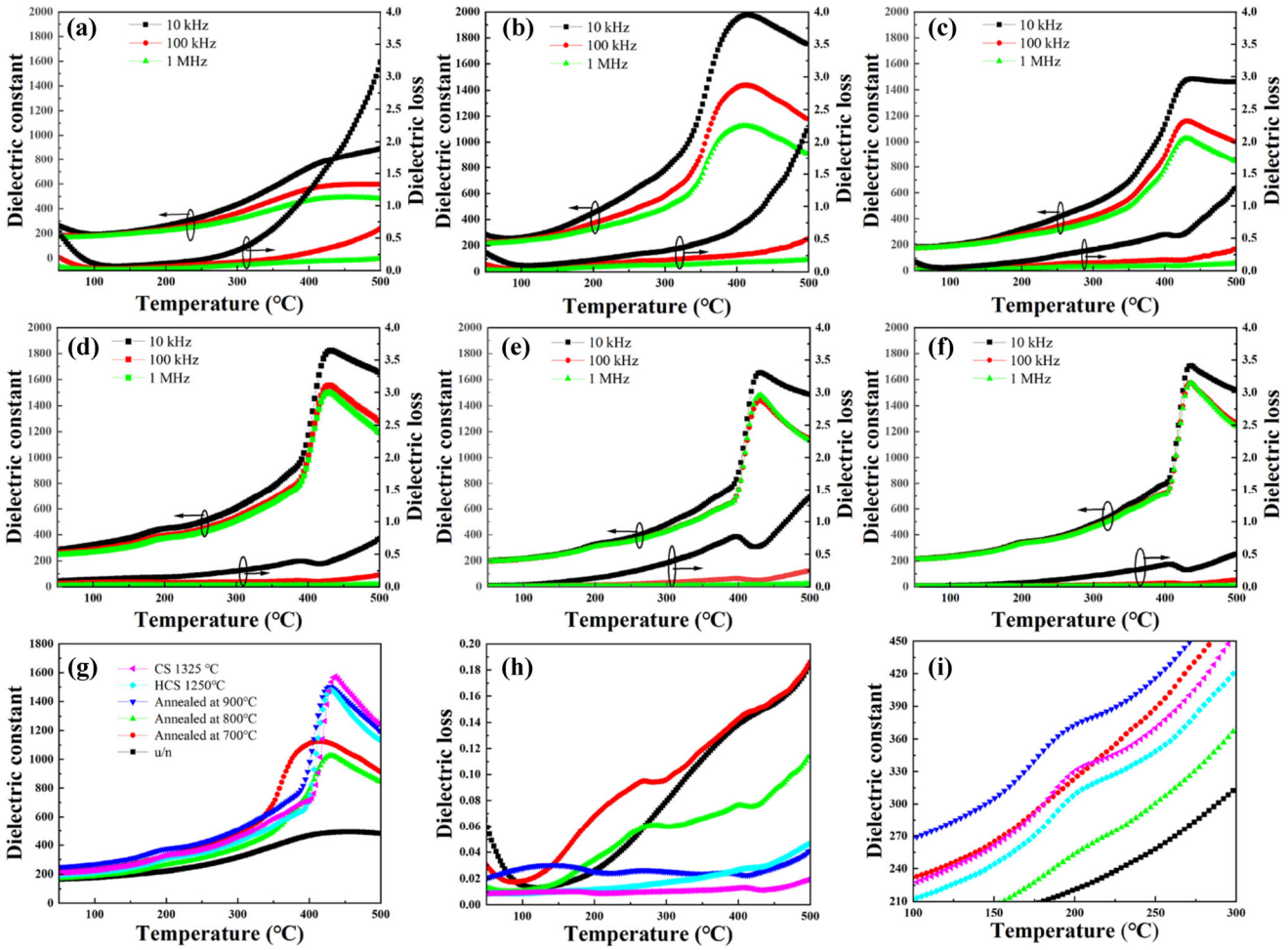

Fig. 7 Temperature-dependent dielectric properties. **a** cold sintered without annealing; **b** cold sintered with annealing at 700 °C; **c** cold sintered with annealing at 800 °C; **d** cold sintered with annealing at 900 °C; **e** HCS prepared; **f** CS prepared; **g** the comparison of dielectric constant at 1 MHz; **h** the comparison of dielectric loss at 1 MHz; **i** the comparison of local dielectric constant at 100–200 °C

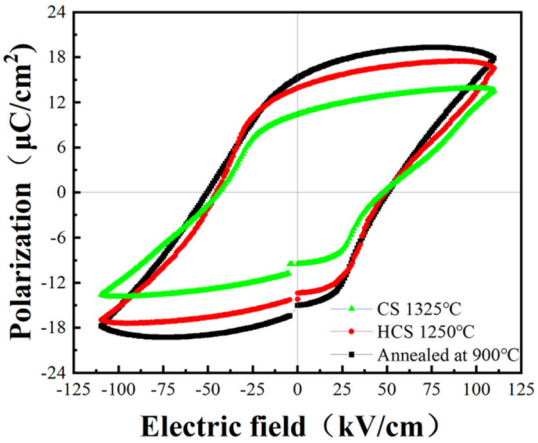

Fig. 8 P-E loops of 900 °C annealed, HCS prepared, and CS prepared ceramics

Funding

The work was supported by the National Natural Science Foundation of China (Grant No. 11704242) and the Natural Science Foundation of Shanghai, China (Grant No. 17ZR1447200).

Data availability

All data generated or analyzed during this study are included in this article.

Declarations

Conflict of interest The authors declare that they have no competing financial interests.

References

1. H. Liu, B. Dkhil, J. Mater. Sci. **52**, 6074 (2017)
2. H. Liu, Ceram. Int. **46**, 8255 (2020)
3. X. Wu, H. Liu, J. Chen, J. Mater. Res. **36**, 1153 (2021)
4. Y. Sun, H. Liu, F. Liu, G. Liu, J. Mater. Sci. Mater. Electron. **32**, 21188 (2021)
5. H. Liu, B. Dkhil, Z. Kristallogr. **226**, 163 (2011)
6. Z. Liu, T. Lu, J. Ye, G. Wang, X. Dong, R. Withers, Y. Liu, Adv. Mater. Technol. **3**, 1800111 (2018)
7. H. Liu, Ceram. Int. **45**, 10380 (2019)
8. H. Liu, J. Am. Ceram. Soc. **101**, 5281 (2018)
9. D. Yang, J. Gao, L. Shu, Y.-X. Liu, J. Yu, Y. Zhang, X. Wang, B.-P. Zhang, J.-F. Li, J. Mater. Chem. A **8**, 23724 (2020)
10. H. Qi, A. Xie, J. Fu, R. Zuo, Acta Mater. **208**, 116710 (2021)
11. B. Luo, H. Dong, D. Wang, K. Jin, J. Am. Ceram. Soc. **101**, 3460 (2018)
12. H. Shimizu, H. Guo, S.E. Reyes-Lillo, Y. Mizuno, K.M. Rabe, C.A. Randall, Dalton Trans. **44**, 10763 (2015)
13. H. Qi, R. Zuo, A. Xie, A. Tian, J. Fu, Y. Zhang, S. Zhang, Adv. Func. Mater. **29**, 1903877 (2019)
14. J. Koruza, B. Malič, M. Kosec, J. Am. Ceram. Soc. **94**, 4174 (2011)
15. E.L. Dunning, *The Thermodynamic and Transport Properties of Sodium and Sodium Vapor* (Argonne National Lab, IL, 1960)
16. R.H. Lamoreaux, D.L. Hildenbrand, J. Phys. Chem. Ref. Data **13**, 151 (1984)
17. H. Shimizu, K. Kobayashi, Y. Mizuno, C.A. Randall, J. Am. Ceram. Soc. **97**, 1791 (2014)
18. H. Guo, A. Baker, J. Guo, C.A. Randall, J. Am. Ceram. Soc. **99**, 3489 (2016)
19. J. Guo, H. Guo, A.L. Baker, M.T. Lanagan, E.R. Kupp, G.L. Messing, C.A. Randall, Angew. Chem. Int. Ed. **55**, 11457 (2016)
20. Z. Xie, H. Liu, Ceram. Int. **46**, 6955 (2020)
21. X. Tang, N. Luo, Q. Feng, X. Chen, Y. Wei, J. Alloys Compd **877**, 160284 (2021)
22. M.-H. Zhang, L. Fulanović, S. Egert, H. Ding, P.B. Groszewicz, H.-J. Kleebe, L. Molina-Luna, J. Koruza, Acta Mater. **200**, 127 (2020)
23. S. Lanfredi, M.H. Lente, J.A. Eiras, Appl. Phys. Lett. **80**, 2731 (2002)
24. Y. Xu, H. Liu, J. Mater. Sci. Mater. Electron. **31**, 5221 (2020)
25. X. Tan, C. Ma, J. Frederick, S. Beckman, K.G. Webber, J. Am. Ceram. Soc. **94**, 4091 (2011)
26. C.N.W. Darlington, H.D. Megaw, Acta Crystallogr. B **29**, 2171 (1973)
27. A.M. Glazer, H.D. Megaw, Philosoph. Mag. **25**, 1119 (1972)
28. A.M. Glazer, H.D. Megaw, Acta Cryst. A **29**, 489 (1973)
29. J. Koruza, P. Groszewicz, H. Breitzke, G. Buntkowsky, T. Rojac, B. Malič, Acta Mater. **126**, 77 (2017)
30. Y.I. Yuzyuk, P. Simon, E. Gagarina, L. Hennet, D. Thiaudière, V.I. Torgashev, S.I. Raevskaya, I.P. Raevskii, L.A. Reznitchenko, J.L. Sauvajol, J. Phys. Condens. Matter. **17**, 4977 (2005)
31. H. Guo, H. Shimizu, C.A. Randall, Appl. Phys. Lett. **107**, 112904 (2015)
32. H. Ge, Y. Hou, C. Xia, M. Zhu, H. Wang, H. Yan, J. Am. Ceram. Soc. **94**, 4329 (2011)
33. K. Konieczny, Mater. Sci. Eng. B **60**, 124 (1999)
34. R.H. Dungan, R.D. Golding, J. Am. Ceram. Soc. **47**, 73 (1964)
35. P. Vousden, Acta Crystallogr. A **5**, 690 (1952)
36. G. Shirane, R. Newnham, R. Pepinsky, Phys. Rev. **96**, 581 (1954)
37. L.A. Reznitchenko, A.V. Turik, E.M. Kuznetsova, V.P. Sakhnenko, J. Phys. Condens. Matter **13**, 3875 (2001)